

COSMOGLOBE DR2. II. CIB monopole measurements from COBE-DIRBE through global Bayesian analysis

D. J. Watts^{1*}, M. Galloway¹, E. Gjerløw¹, M. San¹, R. Aurvik¹, A. Basyrov¹, L. A. Bianchi¹, A. Bonato², M. Brilenkov¹, H. K. Eriksen¹, U. Fuskeland¹, K. A. Glasscock¹, L. T. Hergt³, D. Herman¹, J. G. S. Lunde¹, A. I. Silva Martins¹, D. Sponseller⁴, N.-O. Stutzer¹, R. M. Sullivan¹, H. Thommesen¹, V. Vikenes¹, I. K. Wehus¹, and L. Zapelli^{2,5,6}

¹ Institute of Theoretical Astrophysics, University of Oslo, Blindern, Oslo, Norway

² Dipartimento di Fisica, Università degli Studi di Milano, Via Celoria, 16, Milano, Italy

³ Laboratoire de Physique des 2 infinis – Irène Joliot Curie (IJCLab), Orsay, France

⁴ Department of Space, Earth and Environment, Chalmers University of Technology, Gothenburg, Sweden

⁵ Università di Trento, Università degli Studi di Milano, CUP E66E23000110001

⁶ INFN sezione di Milano, 20133 Milano, Italy

January 12, 2026

ABSTRACT

We derive new constraints on the Cosmic Infrared Background (CIB) monopole spectrum from a set of reprocessed COBE-DIRBE sky maps that have lower instrumental and astrophysical contamination than the legacy DIRBE maps. These maps have been generated through a global Bayesian analysis framework that simultaneously fits cosmological, astrophysical, and instrumental parameters, as described in a series of papers collectively referred to as COSMOGLOBE Data Release 2 (DR2). We have applied this method to the (time-ordered) DIRBE Calibrated Individual Observations (CIO), complemented by selected HFI and FIRAS sky maps to break key astrophysical degeneracies, as well as WISE and *Gaia* compact object catalogs. In this paper, we focus on the CIB monopole constraints that result from this work. We report positive detections of an isotropic signal in six out of the ten DIRBE bands (1.25, 2.2, 3.5, 100, 140, and 240 μm). For the 2.2 μm channel, we find an amplitude of $10.2 \pm 1.2 \text{nW m}^{-2} \text{sr}^{-1}$, which is 74 % lower than that reported from the official DIRBE maps. For the 240 μm channel, we find $6 \pm 3 \text{nW m}^{-2} \text{sr}^{-1}$, which is 56 % lower than the official DIRBE release. We interpret these lower values as resulting from improved zodiacal light and Galactic foreground modeling. For the bands between 4.9 and 60 μm , the presence of excess radiation in solar-centric coordinates reported in a companion paper precludes the definition of lower limits. However, the analysis still provides well-defined upper limits. For the 12 μm channel, we find an upper 95 % confidence limit of $55 \text{nW m}^{-2} \text{sr}^{-1}$, more than a factor of eight lower than the corresponding legacy result of $468 \text{nW m}^{-2} \text{sr}^{-1}$. The results presented in this paper redefine the state-of-the-art CIB monopole constraints from COBE-DIRBE, and provide a real-world illustration of the power of global end-to-end analysis of multiple complementary data sets which is the foundational idea of the COSMOGLOBE project.

Key words. Zodiacal dust, Interplanetary medium, Cosmology: cosmic background radiation

Contents

1 Introduction

2 Algorithms

3 CIB residual maps and confidence masks

3.1	Data overview
3.2	Implications of excess static radiation
3.3	Half-mission CIB residual maps
3.4	Confidence masks and quality assessment

4 Results

4.1	Burn-in and Monte Carlo convergence
4.2	Monopole constraints
4.3	Comparison with previous results

5 Conclusions

1. Introduction

1 Updates: Zodi oversubtraction is no longer upper limits in the same way as before. Bands 4–7 (check). Bands 4–7 should basically be removed in the monopole overview paper. The table will also be simplified.

4 The Cosmic Infrared Background (CIB) has long been recognized as a key probe of star formation and cosmological large-scale structures (Partridge & Peebles 1967). The unresolved radiation from distant galaxies can be used to probe both the total number density of galaxies at the peak of star formation as well as their clustering properties. Unlike the Cosmic Microwave Background (CMB), whose serendipitous discovery was due to its high photon number density (Penzias & Wilson 1965), the CIB’s total brightness is much fainter, with comparable total brightness to the thermal emission from dust particles in the Milky Way and our own Solar system. Searches from balloons (e.g., Hofmann & Lemke 1978) and sounding rockets (e.g., Matsumoto et al. 1988 and Noda et al. 1992) were limited by local sources of radiation, including the atmosphere and rocket exhaust. As a result, the CIB long eluded direct searches until a series of detector technology breakthroughs in the infrared fre-

11

* Corresponding author: D. Watts; duncan.watts@astro.uio.no

quency regime led to its eventual detection. Specifically, the first detection of the CIB monopole was made by [Puget et al. \(1996\)](#) by combining COBE-FIRAS data between 400–1000 μm with H i measurements to subtract Galactic dust emission. These measurements were later independently confirmed through various other techniques and data sets (e.g., [Fixsen et al. 1998](#); [Schlegel et al. 1998](#); [Lagache et al. 1999](#); [Matsumoto et al. 2005](#); [Matsuura et al. 2011](#); [Pénin et al. 2012](#); [Tsumura et al. 2013](#); [Matsuura et al. 2017](#)).

The first satellite instrument that was specifically designed to detect and characterize both the CIB monopole and fluctuations was the Diffuse Infrared Background Experiment (DIRBE; [Hauser et al. 1998](#)), which flew on-board the NASA-led Cosmic Background Explorer (COBE) satellite. DIRBE continuously observed the infrared sky in ten wavelength bands between 1.25 and 240 μm for about 10 months. In retrospect, and according to subsequent measurements by later experiments such as *Spitzer* ([Dole et al. 2006](#)) and *Planck* (e.g., [Planck Collaboration XXX 2014](#); [Planck Collaboration Int. XLVIII 2016](#)), DIRBE did in fact have the raw sensitivity that was required to make a definitive measurement of both the CIB monopole and anisotropies ([Boggess et al. 1992](#); [Hauser et al. 1998](#)). However, local astrophysical emission in the form of starlight and thermal dust emission from the Milky Way and zodiacal dust emission from the Solar system proved to be an enormous modeling challenge. At the same time, these data opened up an entirely new window for modeling these phenomena, and great efforts were spent on establishing increasingly accurate models. For instance, by establishing a three-dimensional model of dust particles in the Solar system, [Kelsall et al. \(1998\)](#) derived a ground-breaking model of zodiacal light (referred to as K98) from the time-ordered DIRBE data that to this date serve as a standard reference. Similarly, using the DIRBE 100 μm frequency map as a template, [Arendt et al. \(1998\)](#) modeled thermal dust emission in the Milky Way to high enough precision that [Hauser et al. \(1998\)](#) could robustly report measurements of the CIB monopole at 140 and 240 μm . For short wavelengths between 1 and 25 μm , [Arendt et al. \(1998\)](#) established a model for starlight emission that led to unprecedented upper limits on the CIB monopole spectrum. These analyses were quickly followed up by many other authors who leveraged supplementary data sets, turning the original upper limits into positive detections at both 2.2 μm ([Wright & Reese 2000](#); [Gorjian et al. 2000](#); [Wright 2001](#)) and 3.5 μm ([Dwek & Arendt 1998](#); [Gorjian et al. 2000](#); [Wright & Reese 2000](#)). Other contemporary analyses were performed, but the results were never fully corroborated and confirmed as fully isotropic signals; see, e.g., [Hauser & Dwek \(2001\)](#) for a comprehensive review of these early efforts. A recent analysis by [Sano et al. \(2020\)](#) utilized the DIRBE Solar elongation maps to disentangle the isotropic zodiacal emission from the CIB, highlighting the DIRBE dataset's continued relevance in the search for the CIB.

Despite these massive efforts in terms of astrophysical modeling, the final foreground residuals turned out to be too large to allow robust CIB measurements across the full DIRBE wavelength range. For instance, while the K98 model was a huge leap forward in terms of understanding the zodiacal light emission, it still only had a $\sim 99\%$ accuracy. Given that the absolute level of zodiacal light emission at 25 μm is 60 MJy sr $^{-1}$, the corresponding monopole upper limit reported by [Hauser et al. \(1998\)](#) was 0.5 MJy sr $^{-1}$, two orders of magnitude higher than the theoretically predicted CIB monopole. Similarly, residual starlight emission precluded a definitive detection in the near-infrared regime, while residual thermal dust emission from the Milky Way resulted in large uncertainties in the far infrared regime.

Since the DIRBE data were made public in 1996, many other experiments have dramatically improved our knowledge of the 4π infrared sky, including WISE ([Wright et al. 2010](#)), *Planck* HFI ([Planck Collaboration III 2020](#)), and *Gaia* ([Gaia Collaboration et al. 2016](#)). Each of these provide key ancillary information that may be useful to extract CIB information from DIRBE. For instance, *Planck* provides an unprecedented view of Galactic thermal dust, both in terms of sensitivity and angular resolution; WISE provides the location and normalization of Galactic compact objects in the same infrared wavelengths as DIRBE; while *Gaia* provides a detailed parameter library which can be used to model the spectral energy distribution (SED) of many of the stars in their catalogue, and either through direct use of these models, or reasonable extrapolation to similar stars, the SED of virtually every star measured by DIRBE can be modeled ([Galloway et al. 2026](#)).

Not only has there been made great observational breakthroughs since the time of the DIRBE release, but this progress has also been accompanied closely by corresponding efforts in algorithm development. One striking example of this is the field of cosmic microwave background (CMB) analysis, which during more than three decades have established a wide range of highly efficient tools to search for weak signals in data that are contaminated by instrumental noise, astrophysical foregrounds, and systematics (e.g., [Bennett et al. 2013](#); [BICEP2/Keck Array and Planck Collaborations 2015](#); [Planck Collaboration I 2020](#)). One specific branch of this community-wide effort focused on so-called global Bayesian analysis ([Jewell et al. 2004](#); [Wandelt et al. 2004](#)), ultimately culminating in the COSMOGLOBE¹ project which aims to create a single coherent sky model from as many complementary state-of-the-art experiments as possible. The first application of this framework was described in COSMOGLOBE Data Release 1 (DR1; [Watts et al. 2023](#)), which performed the first joint analysis of time-ordered data from both the Wilkinson Microwave Anisotropy Probe (WMAP; [Bennett et al. 2013](#)) and *Planck* LFI ([Planck Collaboration II 2020](#); [BeyondPlanck Collaboration 2023](#)).

In the current COSMOGLOBE DR2 data release, we apply the same process to the DIRBE data with the goal of characterizing the CIB monopole spectrum from 1 to 240 μm . Even after this work, several key problems remain that will require further investigation, both in terms of astrophysical and instrumental modeling. The following results therefore are not the definitive results that ultimately can be derived from DIRBE. Rather, they are the first step in a long process, in which the CIB is gradually being harnessed through the same Bayesian end-to-end methods that have proven effective for analyzing CMB experiments, with the ultimate goal of seamlessly merging the two fields. Two natural next steps in this process are, first, to include high-resolution experiments such as IRAS ([Neugebauer et al. 1984](#)) and AKARI ([Murakami et al. 2007](#)) that can break important degeneracies in the current zodiacal light model, and, second, to reprocess the *Planck* HFI measurements at the level of raw TOD; preliminary steps towards both of these projects have recently been made, and volunteers are welcome to join this Open Source effort.

The rest of the paper is organized as follows. We start by briefly reviewing the overall COSMOGLOBE DR2 data processing algorithm in Sect. 2 and the data in Sect. 3. The corresponding CIB monopole constraints are discussed in Sect. 4. We conclude in Sect. 5, where we also discuss both potential future improvements and the impact of external data.

¹ <https://cosmoglobe.uio.no>

2. Algorithms

The main data set used in this paper is the zodiacal light subtracted DIRBE frequency maps described by Watts et al. (2024). In this section, we briefly review the algorithm that was used to generate these maps.

The first task in any end-to-end Bayesian COSMOGLOBE-style analysis is to write down an explicit parametric model for the raw time-ordered data. For the current DIRBE-targeted analysis, we adopt the following model (Watts et al. 2024),

$$\mathbf{d} = \mathbf{GP} \left[\mathbf{B} \sum_{c=1}^{n_{\text{comp}}} \mathbf{M}_c \mathbf{a}_c + \mathbf{s}_{\text{zodi}} + \mathbf{s}_{\text{static}} \right] + \mathbf{n}, \quad (1)$$

$$\equiv \mathbf{s}^{\text{tot}} + \mathbf{n}. \quad (2)$$

In this expression, \mathbf{d} denotes a stacked vector of the DIRBE Calibrated Individual Observations (CIO) for each frequency band; in the following, we will refer to these as time-ordered data (TOD), following the CMB nomenclature. Next, \mathbf{G} is in principle an $n_{\text{tod}} \times n_{\text{tod}}$ diagonal matrix with an overall constant gain calibration factor per frequency channel; unless otherwise noted, this is usually set to unity, and we mostly adopt the official DIRBE calibration as is.² Moving on, \mathbf{P} denotes the satellite pointing matrix defined in Galactic coordinates, and \mathbf{B} is an instrumental beam convolution operator. Neither of these are associated with any free parameters, but are adopted as perfectly known quantities. The sum runs over n_{comp} astrophysical components, each described by a free amplitude \mathbf{a}_c and a mixing matrix, \mathbf{M}_c , the latter of which is defined by some small number of spectral parameters, β_c ; for full details, see the companion papers Galloway et al. (2026) and Gjerløw et al. (2026). Next, \mathbf{s}_{zodi} denotes zodiacal light emission, which in the current model is described by ~ 70 free parameters collectively denoted ζ_z (San et al. 2024). The static component described by $\mathbf{s}_{\text{static}}$ is extensively discussed by Watts et al. (2024), and we will return to this term in Sect. 3.2; for now, we note that it is described by an amplitude per pixel in solar-centric coordinates, $\mathbf{a}_{\text{static}}$. Finally, \mathbf{n} is Gaussian instrumental noise with free parameters ξ_n , the most important of which are the white noise rms's per time sample for each band.

To complete the data model, we need to specify the astrophysical sky contribution. In the current analysis, we adopt the

following sky model

$$\begin{aligned} \sum_{c=1}^{n_{\text{comp}}} \mathbf{M}_c \mathbf{a}_c &= \mathbf{M}_{\text{mbb}}(\beta_c, T_c, \nu_{0,c}) \mathbf{a}_{\text{cold}} && \text{(Cold dust)} \quad (3) \\ &+ \mathbf{M}_{\text{mbb}}(\beta_h, T_h, \nu_{0,h}) \mathbf{a}_{\text{hot}} && \text{(Hot dust)} \\ &+ \mathbf{M}_{\text{mbb}}(\beta_n, T_n, \nu_{0,n}) \mathbf{t}_{\text{near}} \mathbf{a}_\nu && \text{(Nearby dust)} \\ &+ \left(\frac{\nu_{0,\text{ff}}}{\nu} \right)^2 \frac{g_{\text{ff}}(\nu; T_e)}{g_{\text{ff}}(\nu_{0,\text{ff}}; T_e)} \mathbf{t}_{\text{ff}} && \text{(Free-free)} \\ &+ \delta(\nu - \nu_{0,\text{CO}}^i) \mathbf{t}_{\text{CO}} h_{v,i}^{\text{CO}} && \text{(CO)} \\ &+ \delta(\nu - \nu_{0,\text{CII}}) \mathbf{a}_{\text{CII}} h_\nu^{\text{CII}} && \text{(C II)} \\ &+ U_{\text{mJy}} \sum_{j=1}^{n_s} f_{\text{Gaia},j} \mathbf{a}_{s,j}, && \text{(Bright stars)} \\ &+ U_{\text{mJy}} f_{\text{Gaia},j} \mathbf{a}_{\text{fs},j}, && \text{(Faint stars)} \\ &+ U_{\text{mJy}} \sum_{j=1}^{n_e} M_{\text{mbb}}(\beta_{e,j}, T_{e,j}, \nu_{0,e}) \mathbf{a}_{e,j} && \text{(FIR sources)} \\ &+ m_\nu && \text{(Monopole)}, \end{aligned}$$

where rows describe respectively, from top to bottom, 1) cold dust emission; 2) hot dust emission; 3) nearby dust emission; 4) free-free emission; 5) CO emission; 6) C II emission; 7) bright starlight emission; 8) faint starlight emission; 9) other compact sources; and 10) one monopole for each band. Collectively, we define \mathbf{a}_{sky} to be the set of all signal amplitude maps, and β_{sky} to be the set of all SED parameters. The specific meaning of each symbol in Eq. (3) is not relevant for the present paper, so we refer the interested reader to Galloway et al. (2026) and Gjerløw et al. (2026) for full details.

Finally, we define $\omega = \{\mathbf{G}, \xi_n, \beta_{\text{sky}}, \mathbf{a}_{\text{sky}}, \zeta_z, \mathbf{a}_{\text{static}}\}$ to be the set of all free parameters in the model. Since this model involves a free amplitude per pixel for each foreground model, over hundreds of millions of parameters are being fitted simultaneously, all of which interact non-trivially.

The COSMOGLOBE framework is designed to perform classical Bayesian parameter estimation with a data model such as Eq. (1), and the main goal is then the full joint posterior distribution, $P(\omega | \mathbf{d})$, which is given by Bayes' theorem,

$$P(\omega | \mathbf{d}) = \frac{P(\mathbf{d} | \omega) P(\omega)}{P(\mathbf{d})} \propto \mathcal{L}(\omega) P(\omega). \quad (4)$$

Here $P(\mathbf{d} | \omega) = \mathcal{L}(\omega)$ is called the likelihood, $P(\omega)$ denotes a set of priors, and $P(\mathbf{d})$ is called the evidence, which for our parameter estimation purposes is a normalization constant. The likelihood is defined by the key assumption that the instrumental noise is Gaussian distributed,

$$-2 \ln \mathcal{L}(\omega) = (\mathbf{d} - \mathbf{s}^{\text{tot}}(\omega))^\top \mathbf{N}_w^{-1} (\mathbf{d} - \mathbf{s}^{\text{tot}}(\omega)) \equiv \chi^2(\omega), \quad (5)$$

once again up to a normalization constant. The priors adopted in the COSMOGLOBE DR2 analysis are described by Watts et al. (2024), San et al. (2024), and Galloway et al. (2026), but for this particular paper the most important ones are simply that we assume the CIB and the static components both to be strictly positive.

With these definitions ready at hand, we employ a standard Monte Carlo algorithm called Gibbs sampling (e.g., Geman & Geman 1984) to map out the joint posterior distribution, as implemented in a computer code called Commander (Eriksen et al. 2004; Seljebotn et al. 2019; Galloway et al. 2023). This has already been applied successfully to a wide range of CMB data

² In principle, one could marginalize over the gain uncertainties quoted by the DIRBE team within the Gibbs sampler, but this would increase the Markov chain correlation length significantly. In practice, it is computationally more convenient to propagate these uncertainties analytically into the final results.

sets including *Planck* (Planck Collaboration X 2016; Beyond-Planck Collaboration 2023) and WMAP (Watts et al. 2023). The current analysis is, however, its first application to infrared wavelengths.

Rather than drawing samples directly from a large and complicated joint distribution, in Gibbs sampling one draws samples iteratively from each conditional distribution. For the data model described above, this translates into the following so-called Gibbs chain:

$$G \leftarrow P(G \mid d, \xi_n, \beta_{\text{sky}}, \alpha_{\text{sky}}, \zeta_z, \alpha_{\text{static}}) \quad (6)$$

$$\xi_n \leftarrow P(\xi_n \mid d, G, \beta_{\text{sky}}, \alpha_{\text{sky}}, \zeta_z, \alpha_{\text{static}}) \quad (7)$$

$$\beta_{\text{sky}} \leftarrow P(\beta_{\text{sky}} \mid d, G, \xi_n, \alpha_{\text{sky}}, \zeta_z, \alpha_{\text{static}}) \quad (8)$$

$$\alpha_{\text{sky}} \leftarrow P(\alpha_{\text{sky}} \mid d, G, \xi_n, \beta_{\text{sky}}, \zeta_z, \alpha_{\text{static}}) \quad (9)$$

$$\zeta_z \leftarrow P(\zeta_z \mid d, G, \xi_n, \beta_{\text{sky}}, \alpha_{\text{sky}}, \alpha_{\text{static}}) \quad (10)$$

$$\alpha_{\text{static}} \leftarrow P(\alpha_{\text{static}} \mid d, G, \xi_n, \beta_{\text{sky}}, \alpha_{\text{sky}}, \zeta_z). \quad (11)$$

Here, the symbol \leftarrow indicates the operation of drawing a sample from the distribution on the right-hand side. After some burn-in period, the resulting joint parameter sets will correspond to samples drawn from the true underlying joint posterior.

Each sampling step in this algorithm is described by Watts et al. (2024) and references therein. In some cases, important approximations are made that strictly speaking violate the Gibbs rule, either with the goal of increasing robustness with respect to systematic errors at the cost of increased statistical uncertainties, or simply for algorithmic robustness. A prime example of the former is the fact that our simple model discussed above is not able to fully describe the Galactic plane, and we therefore apply different confidence masks for different applications. An important example of the latter is the zodiacal light model, whose posterior distribution exhibits a large number of local minima due to strong internal parameter degeneracies, and a strict Gibbs sampling algorithm may easily become trapped. For this particular sampling step, we have therefore instead opted for a simple nonlinear Powell algorithm that is initialized some random parameter distance away from the previous sample, and then searches for the local minimum. This algorithm is able to escape local minima, but it comes at the cost of larger uncertainties than what would result from an ideal posterior mapper.

3. CIB residual maps and confidence masks

In this section we give a brief overview of the input datasets that are used as inputs in the COSMOGLOBE DR2 analysis, as well as the output residual maps that serve as the main CIB monopole tracer in the current paper. For full details, we refer the interested reader to Watts et al. (2024).

3.1. Data overview

The calibrated DIRBE TOD forms the primary dataset of interest for COSMOGLOBE DR2. In total, there are 285 days of time-ordered observations at each frequency band, and the total compressed DIRBE data volume is 20 GB. The angular resolution of each band is 42' FWHM due to a common optical design with a field stop for straylight removal, resulting in only small variations between detectors.

The model described by Eqs. (1)–(3) is very rich, and exhibits many strong degeneracies of both instrumental and astrophysical origin. If we were to fit this model to the DIRBE TOD alone, the final solution would become strongly degenerate. To break these degeneracies, we include four other complementary main data sets as part of d (Watts et al. 2024).

Planck HFI: We include one *Planck* HFI PR4 (Planck Collaboration LVII 2020) detector sky map for each of the 100, 143, 217, 353, 545, and 857 GHz frequency bands to constrain the morphology of thermal dust emission. To ensure that neither CMB nor CIB fluctuations from these channels contaminate potential CIB results from DIRBE, we subtract the Commander PR4 CMB temperature map from all channels, as well as the *Planck* PR3 GNILC CIB fluctuation maps (Planck Collaboration et al. 2016) for the 353, 545, and 857 GHz channels; any residual CMB or CIB fluctuations that may remain after these corrections due to modeling uncertainties are much smaller than both thermal dust emission and instrumental noise. The angular resolutions of these sky maps vary between 5 and 10'.

WISE+Gaia: The dominant emission mechanism on short wavelengths is starlight radiation, and many methods have been used to model this in the literature to date. The original DIRBE analysis by Arendt et al. (1998) adopted a phenomenological DIRBE-oriented model that focused on the overall large-scale morphology, while for instance Wright (2001) used 2MASS as a starlight tracer. Since that time, WISE (Wright et al. 2010) and Gaia (Gaia Collaboration et al. 2016) have revolutionized our understanding of starlight emission, and these datasets form the basis of the COSMOGLOBE DR2 model described by Galloway et al. (2026).

COBE-FIRAS: Finally, we also include a subset of the COBE-FIRAS (Mather et al. 1994) sky maps in the current analysis, for two main reasons. First, FIRAS serves as a powerful validation source for the absolute calibration of the DIRBE 140 and 240 μm frequency channel. Second, there is a strong emission line present in the DIRBE 140 μm channel at 158 μm due to C II. By combining high spectral resolution information from FIRAS with high spatial resolution information from DIRBE 140 μm , a novel full-sky C II template is derived as part of the current data release. This component has to our knowledge never been accounted for in previous CIB studies of the DIRBE 140 μm channel.

The computational cost for producing one single Gibbs sample according to the algorithm described in Sect. 2 is about 500 CPU-hrs or 4 wall-hours when run on a 128-core cluster node. In total, we have produced 930 samples for the current analysis, parallelized over six chains, for a total computational cost of 470k CPU-hrs. The first 20 samples are removed as burn-in from each chain (San et al. 2024), leaving a total of 810 samples for scientific analysis. The total wall time was one month.

3.2. Implications of excess static radiation

The parametric model described in Sect. 2 includes a component denoted s_{static} which describes a contribution from excess radiation that appears stationary in solar-centric coordinates. The existence of such excess radiation in the DIRBE data was reported already by Leinert et al. (1998), and illustrated in their Figure 54. The first detailed and systematic study of this effect, however, has only now been performed as part of COSMOGLOBE DR2 (Watts et al. 2024). Since this component plays a particularly critical role in constraining the CIB monopole with DIRBE data, we provide a brief review of the effect here.

Excess radiation that appears stationary in solar-centric coordinates could arise from at least two physical sources. First, any zodiacal light component that actually is stationary in solar-

centric coordinates could obviously be described by this term. Two well-known examples are the so-called “circumsolar ring” and “Earth-trailing feature” in the K98 model (Kelsall et al. 1998), which originate from dust particles trapped in the joint gravitational field of the Earth-Sun system. Another possible source is straylight contamination from the Sun due to telescope non-idealities. As discussed by Hauser et al. (1998), the DIRBE optics were specifically designed to minimize such contamination, and no corrections were made for straylight radiation in the legacy analysis.

Whatever the origin of the excess radiation might be, Watts et al. (2024) have now mapped its spatial structure and amplitude for each DIRBE frequency band by binning the residual TOD, $\mathbf{d} - \mathbf{s}^{\text{tot}}$, into solar-centric coordinates. The strongest signal is found at the $25\,\mu\text{m}$ channel, and this is reproduced in the top panel of Fig. ???. In this figure, the Sun is located in the center, and the equator is aligned with the Ecliptic plane. Dark blue pixels indicate directions that are not observed by the DIRBE instrument. For reference, Kelsall et al. (1998) noted that their zodiacal light model showed significant residuals for solar elongation angles smaller than 68° and larger than 125° , and those observations were excluded from their zodiacal light mission average (ZSMA) maps; those limits are marked as gray lines in Fig. ???. Based on the updated analysis of Watts et al. (2024), it is now in retrospect clear that all the excess signal seen between the two gray lines is in fact present in the final legacy DIRBE ZSMA maps, and has affected all scientific results derived from those sky maps during the last three decades.

Qualitatively similar signals were found at all bands between 4.9 and $100\,\mu\text{m}$, while for wavelengths between 1.25 and $3.5\,\mu\text{m}$ only weak signatures are visible. At the two longer wavelengths, 140 and $240\,\mu\text{m}$, there is no evidence for excess radiation at all. In this respect it is worth noting that the ten DIRBE detectors are divided into three groups in the optical path of the instrument (Silverberg et al. 1993), with the same grouping as observed for the strength of the solar-centric excess signal.

As far as the current paper is concerned, it is irrelevant whether this excess signal is due to a yet-unknown zodiacal light component or straylight from the Sun. Given that its amplitude reaches $5\,\text{MJy sr}^{-1}$, it must in either case be fitted and removed from the raw time-ordered data prior to mapmaking. Given the complex structures seen in Fig. ???, it does not appear satisfactory simply to exclude a fixed range of solar elongations from the final mapmaking, given that the excess reaches several MJy sr^{-1} even at moderate solar elongations.

Since we do not yet have a detailed physical model for the signal, $\mathbf{a}_{\text{static}}$ must be fitted freely pixel-by-pixel in solar-centric coordinates for each frequency band. This, however, introduces a perfect degeneracy between the zero-level of $\mathbf{a}_{\text{static}}$ and the CIB monopole for the affected channels. If one adds an arbitrary offset to the map in the top panel in Fig. ???, and subtracts exactly the same value from the CIB monopole at the same channel, the total goodness-of-fit at that channel is unchanged.

As a temporary solution to this problem, we opted in the current data processing to set the zero-level of the $\mathbf{a}_{\text{static}}$ map at each channel to the lowest possible value that still results in a positive signal within instrumental noise fluctuations. The motivation for this is simplicity of interpretation. Whether the excess signal is due to zodiacal light emission or sidelobes, it should either way be positive, and setting it to the lowest possible value ensures that the final CIB constraints translate into strict upper limits. This is illustrated in the bottom panel of Fig. ???. In this case, we have added an extra offset of $0.8\,\text{MJy sr}^{-1}$ to $\mathbf{a}_{\text{static}}$ at $25\,\mu\text{m}$, or $96\,\text{nW m}^{-2}\,\text{sr}^{-1}$. Both versions of this correction template will

yield an identical overall χ^2 after fitting the monopole m_ν , and both appear as physically plausible at a purely visual level. However, the bottom case will yield a CIB monopole that is lower by $0.8\,\text{MJy sr}^{-1}$. The reason for considering precisely this value here is elaborated on in Sect. 4. Conversely, it is not possible to add a negative offset of $-0.8\,\text{MJy sr}^{-1}$, since the template will then become significantly negative beyond what is allowed by instrumental noise.

At the same time, the “lowest possible zero-level” is not a uniquely defined quantity, but is rather itself uncertain. Indeed, as described by Watts et al. (2024), the specific numerical values adopted for the absolute zero level, $\mathbf{a}_{\text{static,min}}$, in the final COSMOGLOBE DR2 processing were set slightly positive in order to ensure that the Gibbs sampler explored a physically allowed parameter region. The difference between these values and the absolute lowest allowed values were then estimated by convolving the static templates with a series of different smoothing kernels. The uncertainties resulting from these calculations are reproduced in column (f) in Table 1, and we add these in quadrature to the total CIB monopole uncertainty.

In principle, we model the excess static radiation in terms of a free amplitude, $\mathbf{a}_{\text{static}}$, for each pixel in solar-centric coordinate map. This map is fitted independently at each wavelength band between 4.9 and $60\,\mu\text{m}$, but not in the others. However, in practice this component is only fitted freely pixel-by-pixel in the penultimate analysis, as discussed by Watts et al. (2024), due to strong degeneracies with the solar components, and in particular the interplanetary dust cloud. If one lets both the static component and the cloud parameters to be fitted entirely freely, the resulting Markov chain has an extremely long correlation length, and it becomes difficult to assess convergence. To solve this problem, we therefore only fit the static component pixel-by-pixel in a preliminary run, and then project out the modes that are orthogonal to the zodiacal light signal by linear regression, as well as determine its lowest possible zero-level. This results in the template seen in the top panel of Fig. ?? for the $25\,\mu\text{m}$ channel. In the final production analysis, this component is then kept fixed; for full discussion about this procedure, see Watts et al. (2024).

As illustrated in Fig. ??, this template is a high signal-to-noise ratio contribution, and its inclusion does not significantly increase the overall noise level of the main higher-level products. However, since the zero-level of this signal is unknown – up to the requirement that it must be positive – all CIB monopole results derived for the wavelength range between 4.9 and $60\,\mu\text{m}$, for which this correction is applied, are strictly upper limits.

3.3. Half-mission CIB residual maps

By applying the algorithm described in Sect. 2 to the data summarized in Sect. 3.1, we obtain samples from a full joint posterior distribution. However, the primary focus of this paper is the CIB monopole specifically, which, by inspection of Eqs. (1)–(3), is actually not explicitly included in the parametric model at all. Rather, these parameters are only implicitly included in the general monopole parameter, m_ν , which includes all contributions to the monopole, of which the CIB is only one. The appropriate tracer for the CIB monopole in our framework is therefore the following residual map,

$$\mathbf{r}_\nu = \mathbf{d}_\nu - (\mathbf{s}_{\text{tot},\nu} - m_\nu). \quad (12)$$

Ideally, if the assumed parametric model were perfect, this map should consist only of a monopole and instrumental noise.

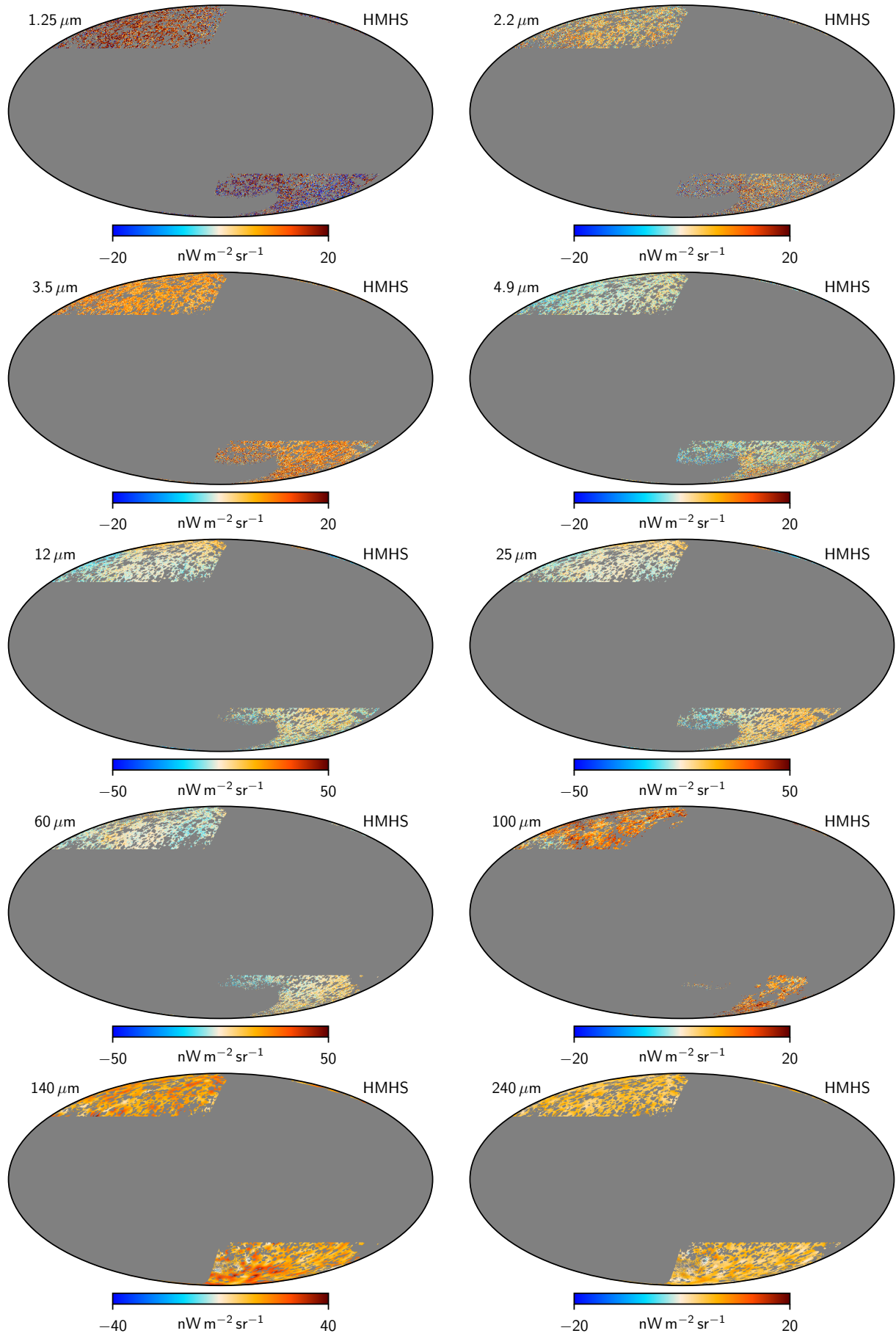


Fig. 1. Half-mission half-sum maps, $(\mathbf{m}_{\text{HM1}} + \mathbf{m}_{\text{HM2}})/2$ for each DIRBE frequency channel. Gray pixels indicate the union of a Galactic mask and the requirement that any pixels must be observed during both HM1 and HM2. The 140 and 240 μm maps have been smoothed to an angular resolution of 3° FWHM.

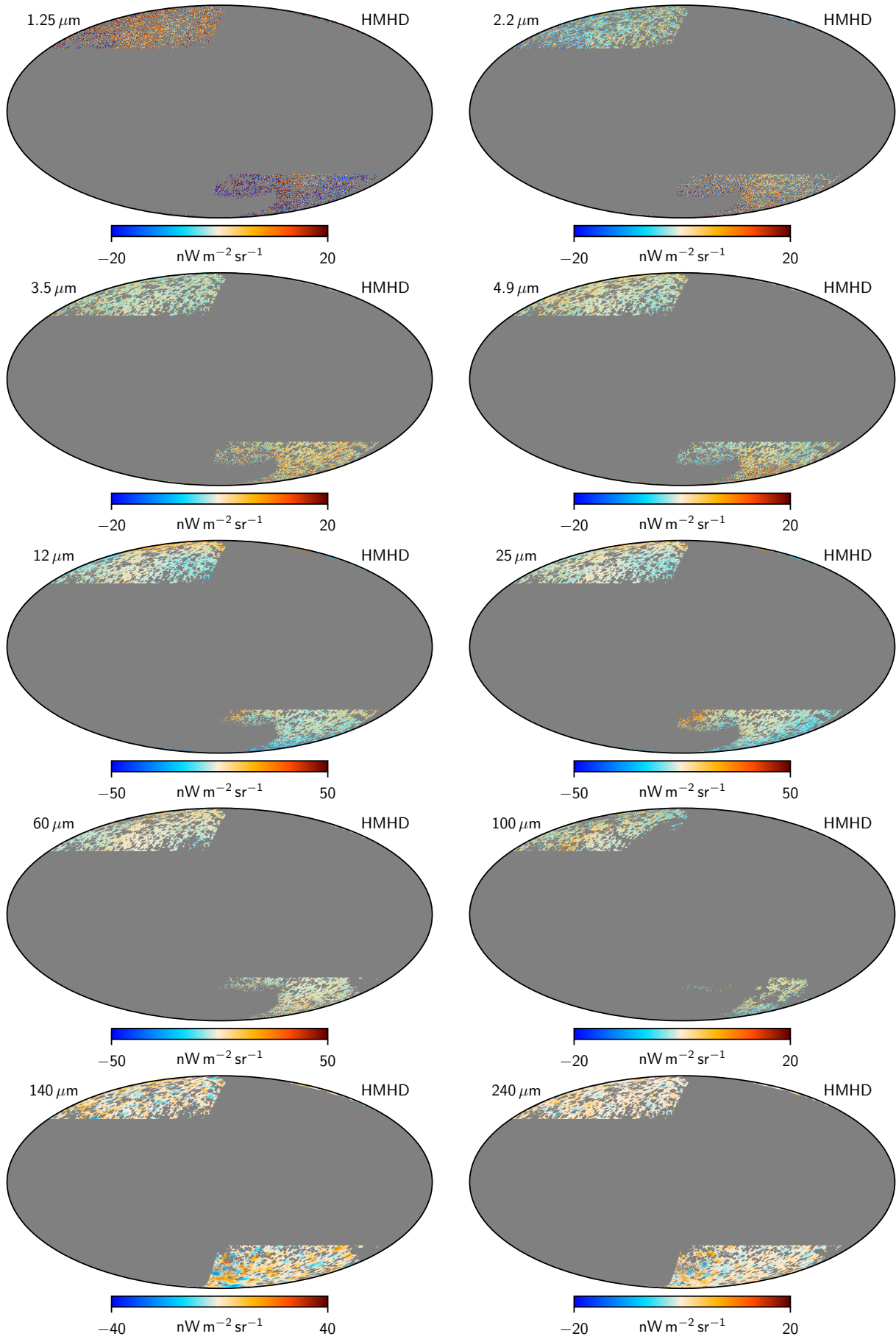


Fig. 2. Half-mission half-difference maps, $(\mathbf{m}_{\text{HM1}} - \mathbf{m}_{\text{HM2}})/2$ for each DIRBE frequency channel. Gray pixels indicate the union of a Galactic mask and the requirement that any pixels must be observed during both HM1 and HM2. The 140 and 240 μm maps have been smoothed to an angular resolution of 3° FWHM.

By computing separate frequency maps for the first and second half of the mission, we obtain two different estimates of the true sky at each frequency. We refer to the first half-mission as HM1 and the second as HM2. We then define the half-mission half-sum (HMHS) and half-mission half-difference (HMHD) maps as follows,

$$\mathbf{r}_v^{\text{HMHS}} = (\mathbf{r}_v^{\text{HM1}} + \mathbf{r}_v^{\text{HM2}})/2 \quad (13)$$

$$\mathbf{r}_v^{\text{HMHD}} = (\mathbf{r}_v^{\text{HM1}} - \mathbf{r}_v^{\text{HM2}})/2. \quad (14)$$

Since the true sky signal should be the same in both maps for an ideal instrument, $\mathbf{r}_v^{\text{HMHS}}$ provides an estimate of the true sky, while $\mathbf{r}_v^{\text{HMHD}}$ provides a combined estimate of both instrumental noise and residual systematics. Most importantly for the current analysis, the HMHD residual map includes a contribution from seasonal modeling errors in the zodiacal light model. At the same time, it is important to note that both HM1 and HM2 are processed simultaneously in the COSMOGLOBE DR2 processing (Watts et al. 2024), and important parameters such as the emissivity and albedo of zodiacal light parameters are shared between the two half-missions, and uncertainties in these are not traced by the HMHD map. In general, uncertainties in parameters that are included in the parametric model are described by the Markov chain variations, while seasonally varying model errors are described by the HMHD map. For full error propagation, both terms must be included.

Figures 1 and 2 show the residual HMHS and HMHD maps, respectively, for one single Gibbs sample. The masks adopted for these figures are defined by two criteria: First, any included pixel must be observed by both HM1 and HM2. Second, pixels with a total Galactic foreground contribution larger than a channel-specific threshold are excluded. We note that both the panel layout and color ranges are identical between the HMHS and HMHD figures, and by switching between the two, one can identify the main features by eye. The bottom two panels have been smoothed to an angular resolution of 3° FWHM to suppress instrumental noise.

Two key features are required in order for these data to support a robust CIB detection, namely 1) a clearly larger positive signal in the HMHS map than in the HMHD map, and 2) that the HMHS signal appears statistically isotropic. At the qualitative level of a visual inspection of Figs. 1 and 2, both of these points appear to hold true for the $1.25, 2.2, 140$, and $240\,\mu\text{m}$ channels. At $3.5\,\mu\text{m}$, there are signs of zodiacal light over-subtraction in the Ecliptic plane, while at $4.9, 12$ and $60\,\mu\text{m}$ the amplitude of the HMHD map is as strong as in the HMHS map. At $25\,\mu\text{m}$, there is a large excess in HMHS, as required, but there is also strong evidence of zodiacal light and other residuals. At $100\,\mu\text{m}$, there is a clear difference between the HMHS and HMHD maps, but there is also clear evidence of residual Galactic emission. However, even at the cursory level of such a visual inspection, there appears to be significant evidence of true CIB monopole signal present in the COSMOGLOBE DR2 residual maps.

3.4. Confidence masks and quality assessment

As seen visually in Figs. 1 and 2, the signal-to-noise ratio with respect to pure instrumental noise alone is massive for all DIRBE channels, and the total uncertainty budget will ultimately be dominated by astrophysical confusion and instrumental systematics. With these observations in mind, we define a conservative set of monopole confidence masks that isolate only the cleanest parts of the sky through four criteria.

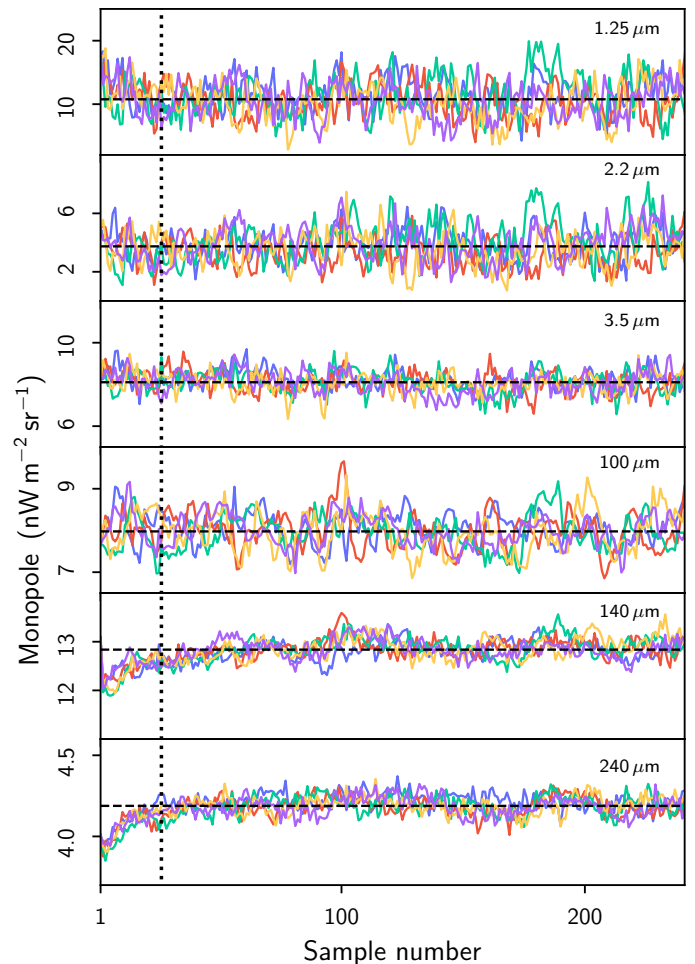


Fig. 3. CIB monopole estimates as a function of Gibbs sample iteration for each DIRBE channel **with a well-defined zero-level**. Each color shows one Markov chain, and the horizontal dashed line shows the final COSMOGLOBE DR2 posterior mean values as tabulated in Table 1. The first 15 samples from each chain have already been removed as burn-in.

First, following the above prescription, we require that any accepted pixel must be observed by both HM1 and HM2. This is a strict requirement in order to be able to use the HMHD maps directly for error propagation over the same sky fraction as used for estimating the signal level itself.

Second, it is evident from Fig. 2 that the Ecliptic plane is particularly susceptible to zodiacal light residuals. We therefore exclude all pixels with an absolute Ecliptic latitude below $|b| < 45^\circ$ from the analysis; this cut excludes 71% of the sky. We have checked that setting the limit at either $|b| < 60^\circ$ or 75° gives very similar results, only with slightly larger Monte Carlo uncertainties.

Third, to remove pixels with obvious modeling failures, we evaluate the so-called χ^2 map of the form

$$\chi_p^2 = \sum_v \left(\frac{d_{v,p} - s_{v,p}^{\text{sky}}}{\sigma_{v,p}} \right)^2, \quad (15)$$

where p is defined at a HEALPix³ grid of $N_{\text{side}} = 512$, corresponding to $7' \times 7'$ pixels (Górski et al. 2005). Contributions from the *Planck* frequency bands, which have four times higher resolution, are co-added into these coarser pixels, and each of the

³ <http://healpix.sourceforge.io>

six *Planck* channels therefore contributes with 16 pixels per χ^2 element. We then smooth this χ^2 map to 1° FWHM, and remove any pixel with a value larger than 200, corresponding roughly to a reduced χ^2 of 1.9; this cut excludes 14 % of the sky. We have checked that increasing the threshold by a factor of two or five does not significantly affect the results.

Finally, we remove any pixels with a large absolute Galactic foreground contribution. For channels between 1.25 and $4.9\,\mu\text{m}$, we exclude any pixels for which the sum of the bright stars and other compact objects (as defined by Eq. 3) evaluated at $1.25\,\mu\text{m}$ is brighter than $20\,\text{kJy sr}^{-1}$, or where the faint starlight template is brighter than $50\,\text{kJy sr}^{-1}$. Combined, these cuts exclude 88 % of the sky. For the six longer-wavelength bands, we exclude any pixels for which the sum of the three dust components is larger than $50\,\text{MJy sr}^{-1}$ evaluated at the pivot frequency of $545\,\text{MJy sr}^{-1}$; this removes 32 % of the sky.

Figures ?? and ?? shows zoom-ins around the North Ecliptic Pole of the same HMHS and HMHD maps plotted in Figs. 1 and 2, but with the new and more conservative analysis masks applied. Similar zoom-ins of around the South Ecliptic Pole are shown in Figs. ?? and ???. Again, when comparing the HMHS and HMHD maps in these figures, the 1.25 , 2.2 , 140 , and $240\,\mu\text{m}$ channels all appear to provide a highly significant detection of an isotropic signal. Indeed, with these more stringent cuts, even the 3.5 and $100\,\mu\text{m}$ channels appear sufficiently clean to justify a direct measurement.

Finally, we note that the $25\,\mu\text{m}$ channel appears rather anomalous in this data set. Specifically, even though it actually appears rather isotropic by visual inspection, it has a higher amplitude than either of the two neighboring channels, namely a value of about $50\,\text{nW m}^{-2}\,\text{sr}^{-1}$ compared to less than $30\,\text{nW m}^{-2}\,\text{sr}^{-1}$ for the 12 and $60\,\mu\text{m}$ channels. Such a rapidly changing monopole spectrum is obviously very difficult to explain in terms of either astrophysics or a cosmological signal. A far more compelling explanation is the uncertainty in the zero-level of the static component shown in Fig. ???. The current results are derived with the default low zero-level template shown in the top panel. However, if the true zero-level of the $25\,\mu\text{m}$ channel should happen to be $0.8\,\text{MJy sr}^{-1}$, the excess seen in Fig. ?? would vanish entirely.

With this visually obvious observation in mind, it is worth re-emphasizing that the same argument applies also to the other channels for which the static template is applied, namely 4.9 – $60\,\mu\text{m}$. By increasing the zero-level of the respective static template, the monopole seen in Fig. ?? can be decreased all the way to zero. However, since the static template has to be positive, the monopole cannot be increased significantly compared to what is seen in Fig. ???. These maps do therefore impose strong upper limits on the CIB monopole in this wavelength range, despite the presence of the static component.

4. Results

4.1. Burn-in and Monte Carlo convergence

As described in Sect. 2, the COSMOGLOBE algorithm is a Gibbs sampler, and is as such subject to Monte Carlo burn-in and convergence. It has to run for long enough to reach a stationary state, and once it does that, it has to explore the full joint posterior distribution for sufficiently long to ensure that the posterior standard deviation is well measured.

Figure 3 shows the mean monopole as a function of Gibbs iteration for each DIRBE channel as evaluated over the confidence masks defined in Sect. 3.4, after removing the first 20 samples in

each chain as suggested by San et al. (2024). The colored lines show results from the six independent Gibbs chains. Based on this plot, we do not see any significant evidence for remaining burn-in, as the chains appear stationary from the very beginning.

As far as Monte Carlo convergence goes, we see that the remaining samples appear to scatter with a relatively short correlation length for all channels at wavelengths shorter than $140\,\mu\text{m}$. However, at the two longest wavelengths the correlation length is very long, and each chain appears to largely explore its own local minimum. As discussed by San et al. (2024), these channels also have a low signal-to-noise ratio with respect to zodiacal light, and there is therefore a strong degeneracy between the band monopole and the zodiacal light emissivity that takes a long time to explore with Gibbs sampling. At the same time, the same analysis also shows that the combination of the six chains does cover the physically plausible range for the zodiacal light emissivities, and the range covered by the monopole chains seen in Fig. 3 therefore also provide a useful estimate of the corresponding physically meaningful monopole uncertainty, despite the long correlation length. Indeed, in a future update of this analysis it might be prudent to impose a physically motivated prior on the zodiacal light emissivity by extrapolating from the 12 – $60\,\mu\text{m}$ channels, and this will then significantly decrease the Monte Carlo uncertainties seen in this figure. For now, however, we prefer the conservative approach, and do not impose any priors on the zodiacal light amplitude, at the cost of increased monopole uncertainties in the far-infrared regime.

4.2. Monopole constraints

We are now finally ready to present one of the main results from the COSMOGLOBE DR2 analysis, namely updated constraints on the CIB monopole spectrum from DIRBE. Based on the above discussions, we provide point measurements at 1.25 , 2.2 , 3.5 , 100 , 140 , and $240\,\mu\text{m}$, while for the remaining channels we provide only upper limits.

For channels with a positive detection, the central value is simply taken as the posterior mean averaged over all accepted Gibbs samples. In contrast, the corresponding uncertainty is significantly more complicated, and includes five different terms added in quadrature. The starting point of the current analysis are the calibrated TOD as provided by the DIRBE team. This process itself has uncertainties both in terms of baseline determination and absolute calibration as listed in Table 2 of Hauser et al. (1998). (1) The baseline is a linear term, and we therefore propagate this directly as provided. (2) However, the gain uncertainty is a multiplicative value in units of percent, and we therefore multiply those uncertainties with our best-fit monopole values for each channel. (3) The third contribution is simply the posterior RMS as evaluated from the Gibbs samples; this quantifies statistical uncertainties that are directly described by the parametric model in Eqs. (1)–(3). The most important examples of such are zodiacal light and astrophysical foreground variations. (4) We then include a fourth contribution defined by the RMS of the HMHD map, downgraded to $N_{\text{side}} = 4$ in order to suppress instrumental noise. This measures modeling errors that are not captured within the model itself, but have a seasonal variation; a typical example of such is zodiacal light mismodeling errors that lead to different signatures in the first and second half of the DIRBE survey. (5) Lastly, we include a term that describes residual uncertainties in the zero-level of the static component. As discussed above, the zero-level of these templates have been set as low as possible without introducing large negative regions. However, this value itself is not unique, but rather depends for

Table 1. Summary of CIB monopole constraints and uncertainties. All monopoles and uncertainties are given in units of $\text{nW m}^{-2} \text{sr}^{-1}$. For channels with a robust monopole detection, the central value corresponds to the posterior mean of all accepted Gibbs samples, and the final DR2 uncertainty is given in column (g); for channels without a robust monopole detection, the upper limit is defined as the sum of the posterior mean value and twice the total uncertainty. The uncertainties given in column (i) are computed as the standard deviation across all accepted Gibbs samples for that channel. The last three rows show the constraints computed on the Southern Hole (SH) as a consistency test.

$\lambda (\mu\text{m})$	$U_{B_\nu \rightarrow \nu I_\nu}^{(\text{a})}$	MONPOLE UNCERTAINTY						CIB MONPOLE CONSTRAINT			
		$\sigma_b^{(\text{b})}$	$\sigma_g^{(\text{c})}$	$\sigma_{\text{MC}}^{(\text{d})}$	$\sigma_{\text{HM}}^{(\text{e})}$	$\sigma_{\text{fg}}^{(\text{f})}$	$\sigma_{\text{Total}}^{(\text{g})}$	DIRBE ^(\text{h})	Gibbs ^(\text{i})	Final DR2 ^(\text{j})	$f_{\text{sky}}^{(\text{k})}(\%)$
1.25	2400	0.05	0.5	2.0	2.5	...	3.2	< 75	12 ± 5	11 ± 3.2	7.6
2.2	1364	0.03	0.1	0.8	2.2	...	2.3	< 39	1.9 ± 1.1	3.7 ± 2.3	7.6
3.5	857	0.02	0.3	0.4	1.8	...	1.9	< 23	6.9 ± 0.6	8.1 ± 1.9	7.6
100	30	0.81	1.0	0.4	0.9	1.3	2.1	< 34	11.0 ± 1.6	8.0 ± 2.1	4.0
140	21	5	1.6	0.4	2.2	1.4	5.9	25.0 ± 6.9	18 ± 6	13 ± 5.9	8.8
240	12	2	0.5	0.1	0.5	0.5	2.2	13.6 ± 2.5	4.3 ± 2.1	4.2 ± 2.2	9.0
100 _{SH}	30	0.81	0.6	0.4	0.002	1.3	1.7	4.6 ± 1.7	1.8
140 _{SH}	21	5	1.2	0.4	0.05	1.4	5.4	11.7 ± 5.4	1.8
240 _{SH}	12	2	0.5	0.2	0.04	0.5	2.1	4.5 ± 2.1	1.8

^a Intensity unit conversion factor, $U_{B_\nu \rightarrow \nu I_\nu} = 3000/\lambda[\mu\text{m}]$, in units of $(\text{nW m}^2 \text{sr}^{-1})/(\text{MJy sr}^{-1})$.

^b CIO baseline (or offset) uncertainty as estimated by the DIRBE team; reproduced from Table 2 of Hauser et al. (1998).

^c CIO gain uncertainty; estimated by multiplying the gain uncertainty in Table 2 of Hauser et al. (1998) with the COSMOGLOBE posterior mean.

^d Statistical Monte Carlo uncertainty estimated as the standard deviation of all accepted Gibbs samples.

^e Rms of the HMHD maps in Fig. 2, downgraded to a HEALPix resolution of $N_{\text{side}} = 4$.

^f Uncertainty due to the hot dust zero-level, estimated to be $1 \mu\text{K}_R$ at 545 GHz.

^g Total monopole uncertainty obtained by adding the individual uncertainties in columns (b)–(f) in quadrature.

^h Official DIRBE monopole constraints reproduced from Table 2 of Hauser et al. (1998).

ⁱ COSMOGLOBE DR2 CIB constraint as derived directly from the monopole parameter in the Gibbs chain; see Watts et al. (2024).

^j COSMOGLOBE DR2 CIB constraint as derived with the tuned monopole masks discussed in Sect. 3.4.

^k Sky fraction used for estimating the final posterior mean monopole with the masks defined in Sect. 3.4.

instance on the intrinsic noise level of the data and the smoothing operator used in the zero-level determination. We therefore assign a residual uncertainty to this value as described by Watts et al. (2024). For channels without a positive detection, we define the upper 95 % confidence limit as the sum of the posterior mean value and two times the total uncertainty.

The results from these calculations are summarized in Table 1, both in terms of individual uncertainty contributions and measurements and upper limits. The final COSMOGLOBE DR2 results are listed in column (j), while the corresponding constraints from Hauser et al. (1998) are reproduced in column (h). As a simple validation test, column (i) lists constraints that are derived directly from the monopole Gibbs samples, m_ν , and these are therefore based on a less conservative masking procedure than the main results. As a further consistency test, we have started an extra Monte Carlo chain splitting the data in even- and odd-numbered scans rather than first and second half of the mission. This led to a larger spatial overlap between the two halves, allowing us to obtain HMHS and HMHD maps of the so-called Southern Hole region. From these we have computed a new set of CIB constraints, reported in the last three rows of Table 1 together with the associated uncertainties, derived through the same steps described above. Overall, the results from these methods are very similar and statistically consistent, illustrating that the final results are not strongly dependent on algorithmic post-processing choices.

Considering the individual contributions to the error budget, we see that different effects dominate for different channels. For instance, the posterior uncertainties dominate at 12 and 25 μm , while at 1.25–3.5 μm the systematic half-mission uncertainties dominate. The ultimate goal is that the statistical term should be the largest factor, and the fact that it not yet is for several

channels indicates that the DIRBE data still have additional constraining power that can be released through further analysis.

4.3. Comparison with previous results

Figure 4 compares the final COSMOGLOBE DR2 constraints with selected previously published results, as well as with a few representative theoretical models. First, the original constraints by Hauser et al. (1998) are shown as orange markers, eight of which are upper limits and two are positive detections. In contrast, our analysis has resulted in several new point estimates as compared to the original analysis, including between 1.25 and 3.5 μm and at 100 μm , while for the four channels spanning 4.9 and 60 μm our limits are generally a factor of two to eight times stronger than the previous results. We also note that for the 140 and 240 μm channels, where Hauser et al. (1998) did report positive detections, our values lower by 64 % and 56 % than the official DIRBE results, respectively. We interpret this as being due to better zodiacal light modeling in COSMOGLOBE DR2, and conclude that the original estimates were biased high by 2–3 σ .

Shortly after the release of the DIRBE analysis, several authors reanalyzed the DIRBE ZSMA maps together with complementary external data sets (e.g., Wright & Reese 2000; Wright 2001), conceptually similar to what is done in the current COSMOGLOBE DR2 release. As two concrete examples, the red points in Fig. 4 show the results obtained by Cambrésy et al. (2001) when combining DIRBE ZSMA at 1.25 and 2.2 μm with 2MASS measurements, while the blue point shows the result derived by Gorjian et al. (2000) at 3.5 μm when combining with dedicated follow-up observations of a $2^\circ \times 2^\circ$ dark spot near the North Galactic Pole. While the latter measurement agrees very well with our measurements, the two former points are higher by

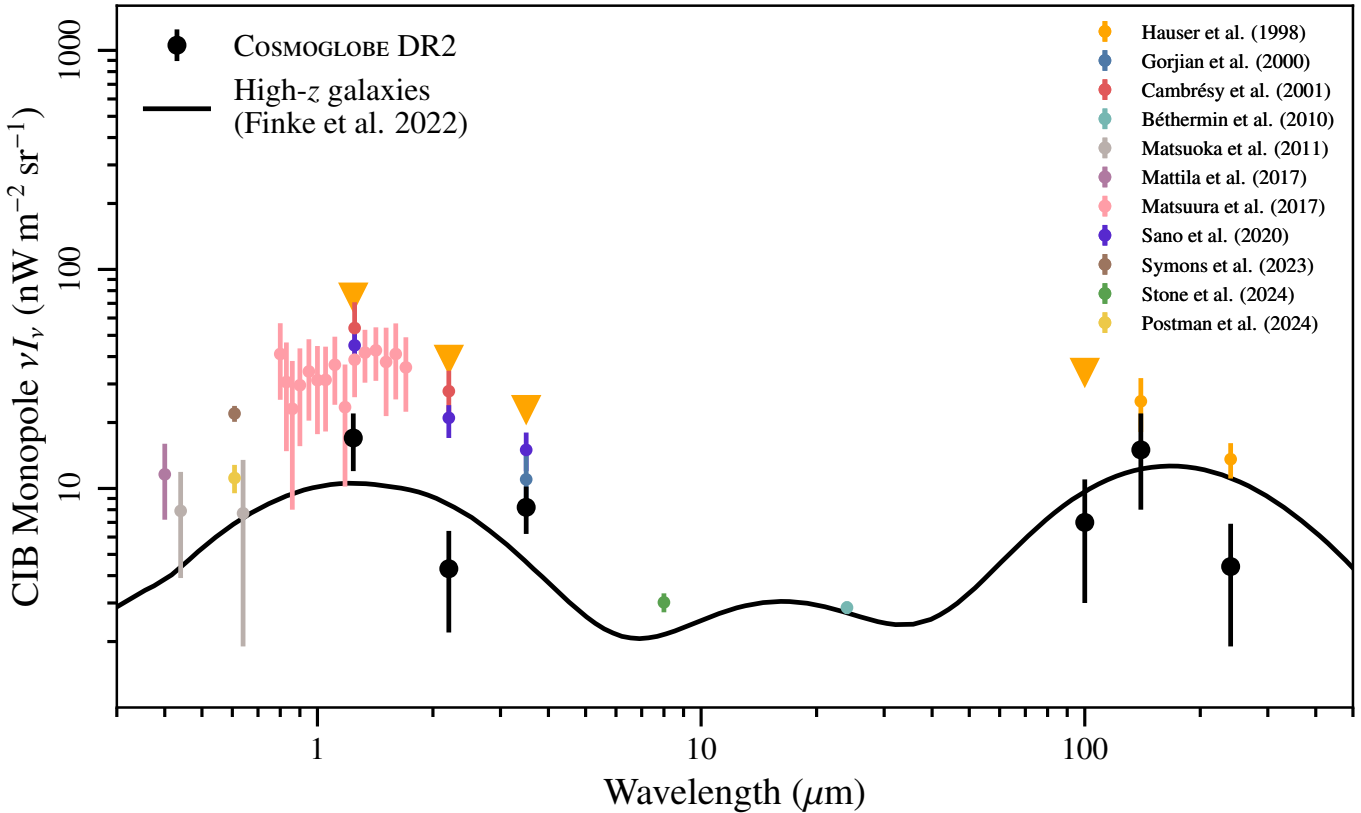


Fig. 4. Comparison of theoretical and observational constraints on the CIB monopole. Black lines include models of integrated galactic background line (Finke et al. 2022) and Population III stars (Santos et al. 2002). Black points show the measurements and upper limits from this work. The orange, blue, red, and dark purple points show independent analyses of the legacy DIRBE maps (Hauser et al. 1998; Gorjian et al. 2000; Cambrésy et al. 2001; Sano et al. 2020), while the cyan and red points show results from *Spitzer* (Béthermin et al. 2010) and *JWST* (Stone et al. 2024). Gray points (Matsuoka et al. 2011) are from the *Pioneer 10* IPP, light purple (Mattila et al. 2017) from ESO VLT, pink (Matsuura et al. 2017) from CIBER, and brown (Symons et al. 2023) and yellow (Postman et al. 2024) from New Horizons. All upper limits are denoted by downward-facing triangles at the 95 % upper limit as calculated in Table 1, while all error bars are 68 % confidence intervals.

25 % and 53 %, respectively, or 1 and 2σ . The other colored points in Fig. 4 correspond to a selection of more recent measurements with other probes. For reference, the continuous line shows the expected contribution of galaxies from redshifts 0–6 as estimated by Finke et al. (2022).

5. Conclusions

In this work, we have derived improved constraints on the CIB monopole spectrum as observed by DIRBE. This was achieved through global end-to-end Bayesian sampling, in which the monopoles were sampled jointly with both zodiacal and Galactic emission and instrumental parameters. The reprocessed DIRBE maps, as presented by Watts et al. (2024), have been improved from the legacy processing in large part due to improved zodiacal dust modeling (San et al. 2024), deeper stellar modeling (Galloway et al. 2026), and a novel thermal dust model (Gjerløw et al. 2026). Notably, the presence of excess radiation that appears static in solar-centric coordinates was identified and removed in the 4.9, 12, 25, and 60 μm bands.

In the current paper we have analyzed a set of data-minus-model residual maps that resulted from this process, which ideally should contain only CIB signal and instrumental noise. Overall, our monopole estimates derived from these maps are significantly lower than those derived from the legacy DIRBE maps. This is true across the entire wavelength band, even at

those channels where significant detections were already reported in the literature. Based on the results presented by Watts et al. (2024) and San et al. (2024), we interpret this primarily as improved zodiacal light modeling in the current processing. We anticipate that these improved results and products will have non-trivial implications for many astrophysical and cosmological analyses that were based on the original DIRBE measurements, and stronger limits may now be imposed on a wide range of physical effects.

This progress has been enabled primarily by two defining features of the COSMOGLOBE framework. The first of these is simply joint analysis of multiple complementary state-of-the-art experiments. In the case of DIRBE, the combination of *Planck* HFI, WISE and *Gaia* data has established a new view of emission from the Milky Way in the form of a single sky model that spans 100 GHz to 1 μm , and this has in turn allowed a deeper mapping of the zodiacal light emission than previously possible. The second defining feature of COSMOGLOBE is the use of modern statistical methods and computing power, which enables global end-to-end modeling of full time-ordered data sets. Intuitively speaking, fitting all parameters at once leads to better estimates of each parameter individually, and such global modeling was simply not computationally feasible when the original DIRBE analysis was performed in the 1990's.

Despite these improvements, there are still outstanding problems and degeneracies that cannot be broken with the data used

in this study. The most important of these is the existence of solar-centric excess radiation in the wavelength channels between 4.9, 12, 25, and 60 μm . A natural next step towards understanding this is to establish a detailed straylight model for the DIRBE instrument, for instance using GRASP (Jönsson et al. 2023). If a detailed physical optics analysis excludes a straylight-based explanation, more complicated zodiacal light models must be considered. Irrespective of the origin of this effect, the addition of time-ordered data from other experiments at similar frequencies and with complementary scan strategies can be used to better determine the 3D structure and absolute brightness of zodiacal dust. In particular, IRAS (Boggess et al. 1992) created nearly full-sky maps at 12, 25, 60, and 100 μm with resolution between 0.5' and 2' FWHM. A full end-to-end joint analysis of IRAS and DIRBE will leverage the unique properties of both datasets, and enable robust characterization of the CIB monopole spanning the entire infrared spectrum. Similarly, other full-sky experiments, including the AKARI (Murakami et al. 2007) and the upcoming SPHEREx (Doré et al. 2014) satellites, will be essential for determining the three-dimensional structure of the zodiacal dust and determining the spectrum of the CIB, and we argue that all of these should ideally be analyzed jointly within a common end-to-end framework like COSMOGLOBE.

Acknowledgements. We thank Tony Banday, Johannes Eskilt, Dale Fixsen, Ken Ganga, Paul Goldsmith, Shuji Matsuura, Sven Wedemeyer, and Janet Weiland for useful suggestions and guidance. The current work has received funding from the European Union's Horizon 2020 research and innovation programme under grant agreement numbers 819478 (ERC; COSMOGLOBE), 772253 (ERC; bRITS2COSMOLOGY), and 101007633 (MSCA; CMBINFLATE). Some of the results in this paper have been derived using healpy (Zonca et al. 2019) and the HEALPix (Górski et al. 2005) package. We acknowledge the use of the Legacy Archive for Microwave Background Data Analysis (LAMBDA), part of the High Energy Astrophysics Science Archive Center (HEASARC). HEASARC/LAMBDA is a service of the Astrophysics Science Division at the NASA Goddard Space Flight Center. This publication makes use of data products from the Wide-field Infrared Survey Explorer, which is a joint project of the University of California, Los Angeles, and the Jet Propulsion Laboratory/California Institute of Technology, funded by the National Aeronautics and Space Administration. This work has made use of data from the European Space Agency (ESA) mission *Gaia* (<https://www.cosmos.esa.int/gaia>), processed by the *Gaia* Data Processing and Analysis Consortium (DPAC, <https://www.cosmos.esa.int/web/gaia/dpac/consortium>). Funding for the DPAC has been provided by national institutions, in particular the institutions participating in the *Gaia* Multilateral Agreement. This paper and related research have been conducted during and with the support of the Italian national inter-university PhD programme in Space Science and Technology. Work on this article was produced while attending the PhD program in PhD in Space Science and Technology at the University of Trento, Cycle XXXIX, with the support of a scholarship financed by the Ministerial Decree no. 118 of 2nd March 2023, based on the NRRP - funded by the European Union - NextGenerationEU - Mission 4 "Education and Research", Component 1 "Enhancement of the offer of educational services: from nurseries to universities" - Investment 4.1 "Extension of the number of research doctorates and innovative doctorates for public administration and cultural heritage" - CUP E66E23000110001.

References

- Arendt, R. G., Odegard, N., Weiland, J. L., et al. 1998, ApJ, 508, 74
 Bennett, C. L., Larson, D., Weiland, J. L., et al. 2013, ApJS, 208, 20
 Béthermin, M., Dole, H., Beelen, A., & Aussel, H. 2010, A&A, 512, A78
 BeyondPlanck Collaboration. 2023, A&A, 675, A1
 BICEP2/Keck Array and Planck Collaborations. 2015, Phys. Rev. Lett., 114, 101301
 Boggess, N. W., Mather, J. C., Weiss, R., et al. 1992, ApJ, 397, 420
 Cambrésy, L., Reach, W. T., Beichman, C. A., & Jarrett, T. H. 2001, ApJ, 555, 563
 Dole, H., Lagache, G., Puget, J. L., et al. 2006, A&A, 451, 417
 Doré, O., Bock, J., Ashby, M., et al. 2014, arXiv e-prints, arXiv:1412.4872
 Dwek, E. & Arendt, R. G. 1998, ApJ, 508, L9
 Eriksen, H. K., O'Dwyer, I. J., Jewell, J. B., et al. 2004, ApJS, 155, 227
 Finke, J. D., Ajello, M., Domínguez, A., et al. 2022, ApJ, 941, 33
 Fixsen, D. J., Dwek, E., Mather, J. C., Bennett, C. L., & Shafer, R. A. 1998, ApJ, 508, 123
 Gaia Collaboration et al. 2016, A&A, 595, A1
 Galloway, M., Andersen, K. J., Aulien, R., et al. 2023, A&A, 675, A3
 Galloway, M. et al. 2026, A&A, in preparation [arXiv:20xx.xxxxx]
 Geman, S. & Geman, D. 1984, IEEE Trans. Pattern Anal. Mach. Intell., 6, 721
 Gjerløw et al. 2026, A&A, in preparation [arXiv:20xx.xxxxx]
 Gorjian, V., Wright, E. L., & Chary, R. R. 2000, ApJ, 536, 550
 Górski, K. M., Hivon, E., Banday, A. J., et al. 2005, ApJ, 622, 759
 Hauser, M. G., Arendt, R. G., Kelsall, T., et al. 1998, ApJ, 508, 25
 Hauser, M. G. & Dwek, E. 2001, ARA&A, 39, 249
 Hofmann, W. & Lemke, D. 1978, A&A, 68, 389
 Jewell, J., Levin, S., & Anderson, C. H. 2004, ApJ, 609, 1
 Jönsson, P., Gaigalas, G., Fischer, C. F., et al. 2023, Atoms, 11, 68
 Kelsall, T., Weiland, J. L., Franz, B. A., et al. 1998, ApJ, 508, 44
 Lagache, G., Abergel, A., Boulanger, F., Désert, F. X., & Puget, J. L. 1999, A&A, 344, 322
 Leinert, C., Bowyer, S., Haikala, L. K., et al. 1998, A&AS, 127, 1
 Mather, J. C., Cheng, E. S., Cottingham, D. A., et al. 1994, ApJ, 420, 439
 Matsumoto, T., Akiba, M., & Murakami, H. 1988, ApJ, 332, 575
 Matsumoto, T., Matsuura, S., Murakami, H., et al. 2005, ApJ, 626, 31
 Matsuoka, Y., Jenaka, N., Kawara, K., & Oyabu, S. 2011, ApJ, 736, 119
 Matsuura, S., Arai, T., Bock, J. J., et al. 2017, ApJ, 839, 7
 Matsuura, S., Shirahata, M., Kawada, M., et al. 2011, ApJ, 737, 2
 Mattila, K., Lehtinen, K., Väistönen, P., von Appen-Schnur, G., & Leinert, C. 2017, MNRAS, 470, 2133
 Murakami, H., Baba, H., Barthel, P., et al. 2007, PASJ, 59, S369
 Neugebauer, G., Habing, H. J., van Duinen, R., et al. 1984, ApJ, 278, L1
 Noda, M., Christov, V. V., Matsuura, H., et al. 1992, ApJ, 391, 456
 Partridge, R. B. & Peebles, P. J. E. 1967, ApJ, 148, 377
 Pénin, A., Lagache, G., Noriega-Crespo, A., et al. 2012, A&A, 543, A123
 Penzias, A. A. & Wilson, R. W. 1965, ApJ, 142, 419
 Planck Collaboration, Aghanim, N., Ashdown, M., et al. 2016, A&A, 596, A109
 Planck Collaboration XXX. 2014, A&A, 571, A30
 Planck Collaboration X. 2016, A&A, 594, A10
 Planck Collaboration I. 2020, A&A, 641, A1
 Planck Collaboration II. 2020, A&A, 641, A2
 Planck Collaboration III. 2020, A&A, 641, A3
 Planck Collaboration Int. XLVIII. 2016, A&A, 596, A109
 Planck Collaboration LVII. 2020, A&A, 643, A42
 Postman, M., Lauer, T. R., Parker, J. W., et al. 2024, arXiv e-prints, arXiv:2407.06273
 Puget, J. L., Aghanim, N., Gispert, R., Bouchet, F. R., & Hivon, E. 1996, in IAU Symposium, Vol. 168, Examining the Big Bang and Diffuse Background Radiations, ed. M. C. Kafatos & Y. Kondo, 447
 San, M. et al. 2024, A&A, in preparation [arXiv:20xx.xxxxx]
 Sano, K., Matsuura, S., Yomo, K., & Takahashi, A. 2020, ApJ, 901, 112
 Santos, M. R., Bromm, V., & Kamionkowski, M. 2002, MNRAS, 336, 1082
 Schlegel, D. J., Finkbeiner, D. P., & Davis, M. 1998, ApJ, 500, 525
 Seljebotn, D. S., Bærlund, T., Eriksen, H. K., Mardal, K. A., & Wehus, I. K. 2019, A&A, 627, A98
 Silverberg, R. F., Hauser, M. G., Boggess, N. W., et al. 1993, in Society of Photo-Optical Instrumentation Engineers (SPIE) Conference Series, Vol. 1919, Infrared Spaceborne Remote Sensing, ed. M. S. Scholl, 180–189
 Stone, M. A., Alberts, S., Rieke, G. H., et al. 2024, arXiv e-prints, arXiv:2405.18470
 Symons, T., Zemcov, M., Cooray, A., Lisse, C., & Poppe, A. R. 2023, ApJ, 945, 45
 Tsumura, K., Matsumoto, T., Matsuura, S., Sakon, I., & Wada, T. 2013, PASJ, 65, 121
 Wandelt, B. D., Larson, D. L., & Lakshminarayanan, A. 2004, Phys. Rev. D, 70, 083511
 Watts, D., Galloway, M., Gjerlow, E., et al. 2024, A&A, submitted [arXiv:2408.10952]
 Watts, D. J., Basyrov, A., Eskilt, J. R., et al. 2023, A&A, 679, A143
 Wright, E. L. 2001, ApJ, 553, 538
 Wright, E. L., Eisenhardt, P. R. M., Mainzer, A. K., et al. 2010, AJ, 140, 1868
 Wright, E. L. & Reese, E. D. 2000, ApJ, 545, 43
 Zonca, A., Singer, L., Lenz, D., et al. 2019, Journal of Open Source Software, 4, 1298